CONFERENCE PRE-PRINT

Experimental Investigation of Energetic Particle Mode near the q = 2 **Surface in EAST**

Ming Xu, Zhiyong Qiu, Haiqing Liu, Hailin Zhao, the EAST Team Institute of Plasma Physics, Chinese Academy of Sciences (ASIPP), Hefei 230031, P.R. China (Dated: 13:56 Sunday 28th September, 2025)

The basic features and excitation conditions of energetic particle mode (EPM) instability have been investigated in EAST. The EPM is preferentially to excite near the q=2 surface, is usually in the off-axis region of $2.02 \le R \le 2.1~m$ in lower field side (LFS), with normalized minor radius of $0.2 \le \rho \le 0.5$. The frequency of EPM downward chirps ranges from 60 to 40 kHz, with each burst typically lasting for $\Delta t < 2~m$ s, namely the corresponding chirping rate is estimated to be $df/dt \ge 15~k$ Hz/ms. Electron density variations modulate the EPM downward chirp burst period, and shorter periods promote fast ion loss. Despite causing fast ion loss, the EPM instability burst coincided with an observed increase in electron temperature. An investigation into the relationship between the EPM and the (m/n=2/1) tearing mode reveals that the EPM might play a significant role in modifying the current profile.

I. INTRODUCTION

Energetic-particle-driven MHD instabilities, such as those caused by fusion-born alpha particles and fast ions from neutral beam injection (NBI) or ion cyclotron resonance heating (ICRH), can degrade confinement. Two types of EP-driven modes can be distinguished. The first type, shear Alfvén wave (SAW), resides in gaps in the Alfvén continuum or just outside, and its properties are determined by the bulk plasma. The second type, energetic particle mode (EPM), resides in the Alfvén continuum if the drive can overcome the damping, and its properties are mainly determined by the characteristics of the energetic particles, e.g., their characteristic orbital frequencies. The relationship between SAW and EPM is documented in Refs [1–3]. Typically, these two types of modes are connected, meaning the fluctuations initially manifest as SAWs before evolving non-linearly into EPMs [4].

A key application of EPM physics was the discovery of the fishbone instability [5–8], a mode featured by an m/n = 1/1 internal kink mode located within the q = 1 surface, where q is safety factor, m, n are the poloidal and toroidal mode numbers respectively. Subsequently, the discovery of the off-axis fishbone mode (OFM) [9–13] represented another EPM instability, this time located within the q = 2 surface. Repetitive bursting events consisting of multiple SAWs or EPMs are easily caused the abrupt large amplitude events (ALEs) [14–16]. The radial outward propagation of the EPM mode structure has been observed in HL-2A [17], providing new evidence for the explanation of EPM avalanche events.

A new type of EPM instability, observed on EAST near the q=2 surface, exhibits fundamental characteristics that differ significantly from those of the OFM and ALE instabilities, which also occur in this region. Firstly, the resonance frequencies of fast ions differ for the EPM on EAST and the conventional OFM. The OFM is driven by the precessional resonance of fast ions, with a theoretical frequency on the order of less than 10 kHz. However, experimental observations on EAST show a frequency of approximately 50 kHz, indicating a significant discrepancy. Secondly, the two phenomena exhibit distinctly different destructive effects on plasma performance. The ALE typically causes a minor collapse event, posing a danger to plasma confinement. Experiments on EAST have revealed that the downward chirp frequency of EPM features a stable burst duration, typically lasting for several seconds. This characteristic contributes to a mitigated destructive effect on the plasma. This paper aims to experimentally investigate of excitation conditions and basic features for this new EPM instability.

II. EXPERIMENTAL RESULTS

The experiments are performed in Experimental Advanced Superconducting Tokamak (EAST), and the major and minor radius are $R \leq 1.9$ m and $a \approx 0.45$ m respectively. The upper single null (USN) magnetic configuration is adopted with elongation $\kappa > 1.6$ at last closed flux surface (LCFS). The core line-integrated electron density $\langle n_{e0} \rangle \sim 4 \times 10^{19} m^{-3}$, and the plasma current $I_p = 0.4$ MA, is predominantly sustained by lower hybrid current driven (LHCD), as detailed in Ref. [18]. The toroidal field strength is $|B_{\phi}| \cdot R = 4.16$ T·m, and the safety factor at the 95% magnetic surface, q_{95} , is greater than or equal to 6. The electron cyclotron resonance heating (ECRH) power is deposited at off-axis region for current magnetic configuration, a condition that is conducive to forming a reversed magnetic shear configuration [19].

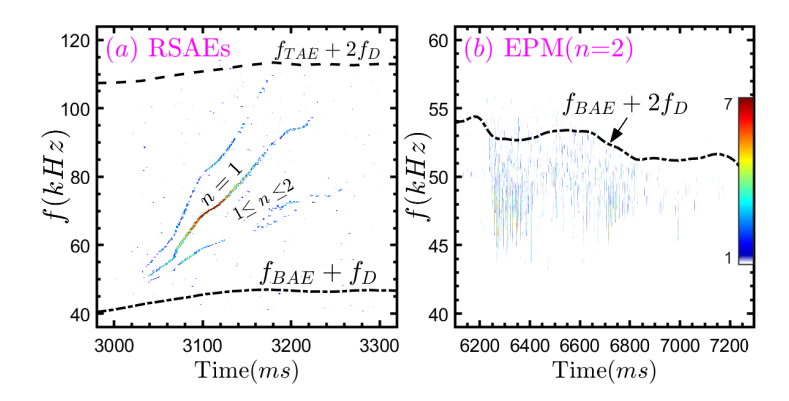


FIG. 1: Upward sweeping RSAEs and downward chirping EPM instabilities are observed near the q = 2 surface, with their frequencies separated by the BAE eigenmode frequency.

Two types of instabilities induced by fast ions are demonstrated in figure 1. The measurements of eigenfrequency of RSAEs (ω_{RSAE}) can be used for determining local value of q_{min} and increasing the accuracy of the EFIT equilibrium reconstruction [20, 21]: $\omega_{RSAE}^2 = v_A^2/R^2 \left(n - m/q_{min}\right)^2 + \omega_{BAE}^2 + \Delta\omega^2$, where $v_A = B/(\mu_0 m_i n_i)^{1/2}$ is the Alfvén speed (ion density $n_i = n_e \approx 3.6 \times 10^{19} m^{-3}$, $v_A \approx 5.3 \times 10^6 m/s$), m_i is the mass of deuterium, R is the major radius, ω_{BAE} is the BAE frequency. The upward sweeping frequency of RSAE starts from the BAE to the gap of toroidal Alfvén eigenmode (TAE), namely the minimum and maximum frequency of RSAE are set by ω_{BAE} and ω_{TAE} respectively, with eigen-frequencies are $\omega_{BAE} \approx (2T_i/m_i)^{1/2} \cdot (7/4 + T_e/T_i)^{1/2}/R$ and $\omega_{TAE} = v_A/(2qR)$ accordingly. Figure 1(a) illustrates the lower boundary of frequency $f_{BAE} + f_D$, while the upper boundary is approximately 110 kHz, corresponding to $f_{TAE} + 2f_D$, where $f = \omega/2\pi$. This establishes the frequency hierarchy as $f_{BAE} < f_{RSAE} < f_{TAE}$. As shown in figure 1(b), the EPM exhibits downward chirping, shifting from the BAE frequency to a lower value, with a frequency shift of $\Delta f \approx 10$ kHz. The EPM instability is clearly captured by the edge magnetic pickup array when the radial position extends to $R \approx 2.1$ m, corresponding to a toroidal mode number of n = 2. In cases with weaker EPM amplitudes, the mode number is typically in the range of $1 \le n \le 2$.

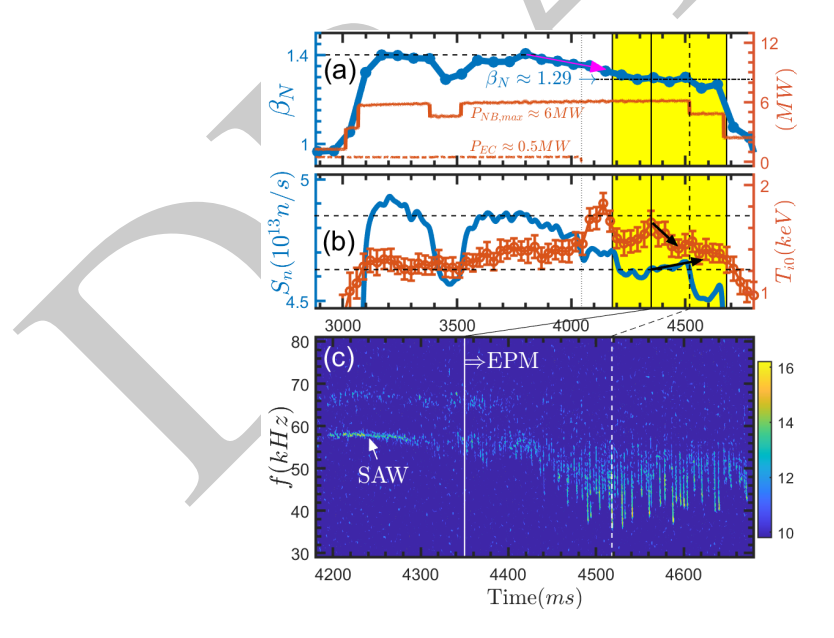


FIG. 2: EPM instability is excited for the condition without ECRH. (a) Normalized beta (β_N) and heating source powers. The powers of NBI and ECRH are shown, with additional contributions from LHCD $(P_{LH} \approx 3 \text{ MW})$ and ICRH $(P_{IC} \approx 1 \text{ MW})$. (b) Neutron yield (S_n) and core ion temperature (T_{i0}) . (c) Spectrogram of ECE signal corresponding to the shaded region in panels (a) and (b).

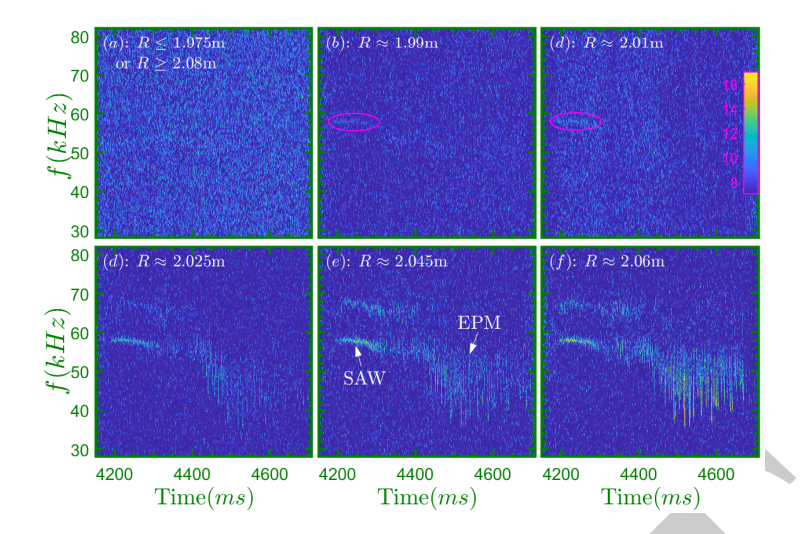


FIG. 3: The radial coverages of the SAW and EPM instabilities are compared.

A. Excitation condition and Comparison with SAW

The excitation condition of EPM instability is demonstrated in figure 2. A maximum normalized beta of $\beta_N \approx$ 1.4 is obtained under the full power configuration of LHCD ($P_{LH} \approx 3$ MW), ECRH ($P_{EC} \approx 0.5$ MW), NBI $(P_{NB} \approx 6 \text{ MW})$, and ICRH $(P_{IC} \approx 1 \text{ MW})$. A gradual decrease in β_N is observed starting at $t \geq 3.8$ s, which precedes the termination of ECRH power at $t \approx 4.05$ s (marked by the magenta arrow). As the β_N value approaches 1.29, two types of fast-ion-induced instabilities are observed, as demonstrated in figure 2(c). The first type instability, exhibiting two frequency branches (f = 58 kHz and 68 kHz), is identified as a SAW mode, which is not discussed further here. The second instability, characterized by a downward frequency chirp from 58 kHz to 38 kHz, is identified as an EPM that consistent with the findings in Ref. [22]. A comparison between these two modes is as follows: (1) Excitation conditions: The EPM is associated with an increase in neutron yield (S_n) and a decrease in core ion temperature (T_{i0}) . In contrast, both parameters decrease for the SAW. (2) Radial positions: The SAW is located within the radial range of $1.98 \le R \le 2.07$ m on LFS. For the EPM, this range shrinks to 2.02 $\leq R \leq 2.07$ m, as shown in figure 3. (3) Plasma Performances: The normalized beta, β_N , for the two modes is nearly identical, at approximately $\beta_N \approx 1.29$. It is important to note that the EPM instability remained unaffected when the NBI power was reduced to $P_{NB} \approx 4.8$ MW ($t \approx 4.52$ s), but it vanished completely at $P_{NB} \approx 2.5$ MW. Therefore, the EPM instability is excited under poor confinement conditions, specifically in discharges without ECRH.

B. Radial positions and Chirp features

The radial position of EPM is demonstrated in figure 4. The EPM instability is concurrently detected by both an edge magnetic pickup array (measuring δB_r) and a core ECE array (measuring δT_e). Analysis of the coherence (γ_{12}) between magnetic and ECE signals reveals that the EPM instability is reliable when $\gamma_{12} \geq 0.3$. The radial location of the EPM instability is found on the lower field side (LFS) within the range of $2.02 \leq R \leq 2.09$ m, in the vicinity of q=2 surface. As β_N or S_n increases, the radial position of EPM instability extends outward ($\Delta r/a$ from 12% to 16%), accompanied by an increase in its fluctuation amplitude. The cross phase-angles differ slightly between the two cases, suggesting that their radial structures are also different.

The basic features of electron temperature fluctuations and downward-chirp frequency of the EPM instability are demonstrated in figure 5. The frequency of EPM downward chirps ranges from 60 to 40 kHz, with each burst typically lasting for $\Delta t < 2$ ms. The corresponding chirping rate is estimated to be $df/dt \geq 15$ kHz/ms. During the growth phase, the $\delta T_e/T_e$ signal is nearly sinusoidal, with its amplitude growing approximately exponentially. The maximum amplitudes for the three cases are identified, yielding growth rates of $\gamma/\omega_0 \simeq 28\%$, 15% and 11% respectively. The time interval between two consecutive EPM burst events is equal to or smaller than 5 ms.

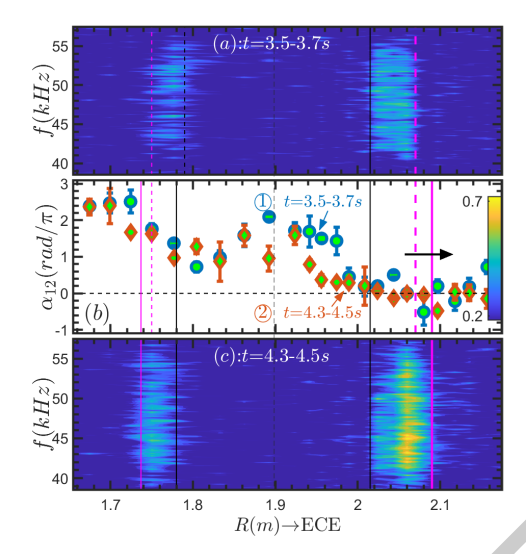


FIG. 4: The coherence γ_{12} between edge magnetic (δB_r) and core ECE (δT_e) signals for two different time intervals of figure 3, as well as the cross-phase angles α_{12} , are demonstrated in (a), (c) and (b), respectively.

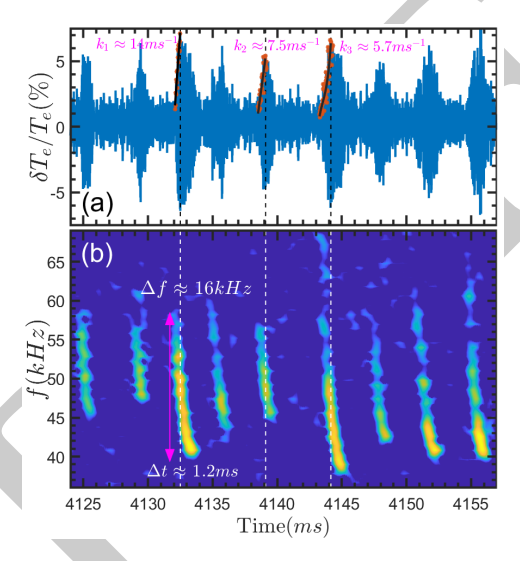


FIG. 5: The fluctuation of $\delta T_e/T_e$ and frequency spectra associated with the EPM instability.

C. Relationship with fast ions

Figure 6 shows that the EPM instability causes the redistribution of fast ions. Two similar discharge conditions are selected, and the β_N value is fully the same as $\beta_N\approx 1.33$. A slight difference in the q-profile between the two cases is inferred from the measured plasma internal inductance (l_i) . The diversity of l_i was obtained by modulating the electron density. The burst period (τ_{dc}) of EPM chirp event is estimated to be approximately 5 ms at a lower electron density ($\langle n_{e0} \rangle \simeq 4 \times 10^{19} m^{-3}$). This period decreases to ≤ 2 ms when the electron density is increased by approximately 6% ($\Delta n_e/n_e \approx 6\%$). As the burst frequency of EPM instability increases (i.e., τ_{dc} decreases), the neutron yield S_n drops by approximately 3%. This indicates that the increases in EPM burst frequency eject more fast ions from the plasma.

From theoretical and experimental analyses, it has been shown that the shearing rate $\omega_{E\times B}$ plays an important role in the suppression of turbulence transport. The $E\times B$ shear rate can be expressed as [23]:

$$\omega_{E \times B} \approx \left| \frac{RB_{\theta}}{B_{\phi}} \frac{\partial}{\partial r} \left(\frac{E_r}{RB_{\theta}} \right) \right| = \left| \frac{r}{q} \frac{\partial}{\partial r} \left(\frac{q}{r} \frac{E_r}{B_{\phi}} \right) \right| \tag{1}$$

where the radial electric field E_r is determined from the ion radial force balance equation [24–26]:

$$E_r = \frac{1}{Zen_i} \frac{dp_i}{dr} - v_\theta B_\phi + v_\phi B_\theta \tag{2}$$

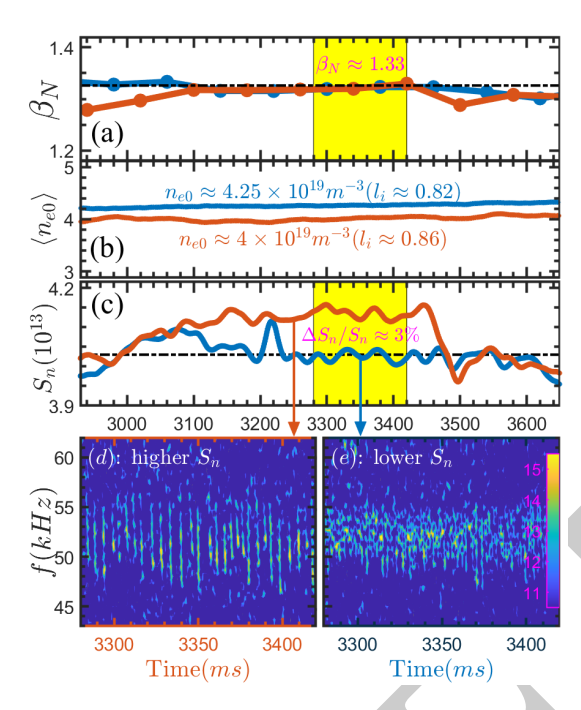


FIG. 6: Comparing the burst frequencies of EPM instability under two similar discharge conditions. The comparison includes: (a) normalized beta (β_N) , (b) core line-integrated electron density $(\langle n_{e0} \rangle)$, (c) neutron yield (S_n) , and the EPM instabilities in the yellow shaded region for each case, shown in (d) and (e) respectively.

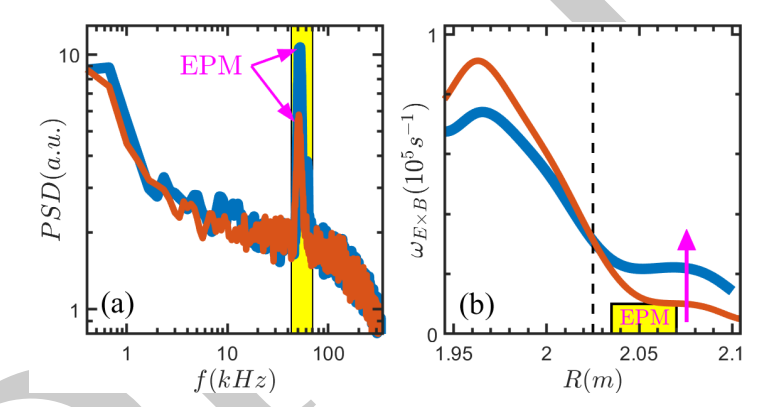


FIG. 7: The $E \times B$ shear flow for the two cases in figure 6 is compared, noting that a higher EPM amplitude corresponds to a higher burst frequency.

the p_i is the ion pressure, v_θ and v_ϕ are the poloidal and toroidal velocities and B_θ and B_ϕ the poloidal and toroidal magnetic fields respectively (safety factor $q=rB_\phi/RB_\theta$), Z is the ion charge number and e the elementary charge. The contribution effect of poloidal flow effect can be predicted by the neoclassical theory, as demonstrated in MAST [27] and NSTX [28]. In current condition, the estimation of the radial electric field (E_r) is primarily based on the consideration of two components: radial ion pressure gradient (∇p_i) and toroidal flow (v_ϕ) items.

The relationship between EPM and $\omega_{E\times B}$ flow shear is investigated in figure 7. The auto power spectra for the two cases are nearly identical, except that a higher EPM burst frequency is associated with a higher fluctuation amplitude at the EPM frequency. Over the major radius range of $1.95 \le R \le 2.1$ m, the $\omega_{E\times B}$ shear rate decreases, exhibiting an inflection point at $R\approx 2.025$ m corresponding to the EPM instability. The $\omega_{E\times B}$ shear rate increases for R>2.025 m and decreases for R<2.025 m with an increase in EPM amplitude, consistent with the EPMs radial location of approximately $2.035 \le R \le 2.07$ m, as marked in figure 7(b). This result is consistent with the finding that EPMs generate zonal flow, as Ref [29]. However, given the identical plasma confinement, the primary factor is likely the reduction in $\omega_{E\times B}$ shear rate observed in the inner region of the EPM instability.

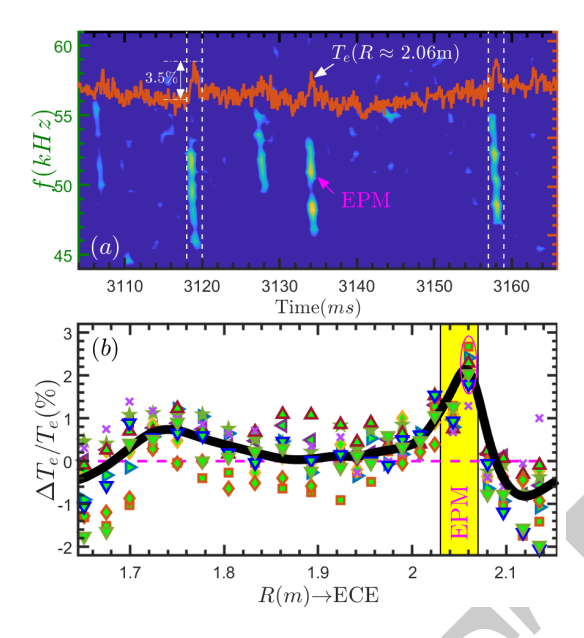


FIG. 8: Relationship between EPM bursts and plasma confinement improvement. (a) Spectrogram and raw signal of ECE; (b) relative temperature alteration induced by EPM instability.

D. Relationship with plasma confinement

The relationship between the burst of EPM instability and the improvement of plasma confinement is illustrated in Figure 8. An abrupt increase in electron temperature T_e is clearly observed during the downward chirping phase of the EPM instability, and T_e drops sharply following the termination of the EPM event. A maximum relative electron temperature increase of $\Delta T_e/T_e \approx 3.5\%$ is recorded. Several cases were analyzed, with a time-averaging window of $\Delta t \approx 0.7$ ms (approximately half the duration of the EPM downward chirping event) applied. The most pronounced variations in $\Delta T_e/T_e$ are observed in two distinct radial regions: $1.73 \le R \le 1.77$ m (HFS) and $2.03 \le R \le 2.07$ (LFS), which correspond to the radial locations of the EPM instability. The maximum averaged value of $\Delta T_e/T_e \approx 2\%$ is recorded at $R \approx 2.06$ m. One plausible explanation is that the zonal flow is excited by the EPM instability [29], leading to the temporal suppression of turbulence.

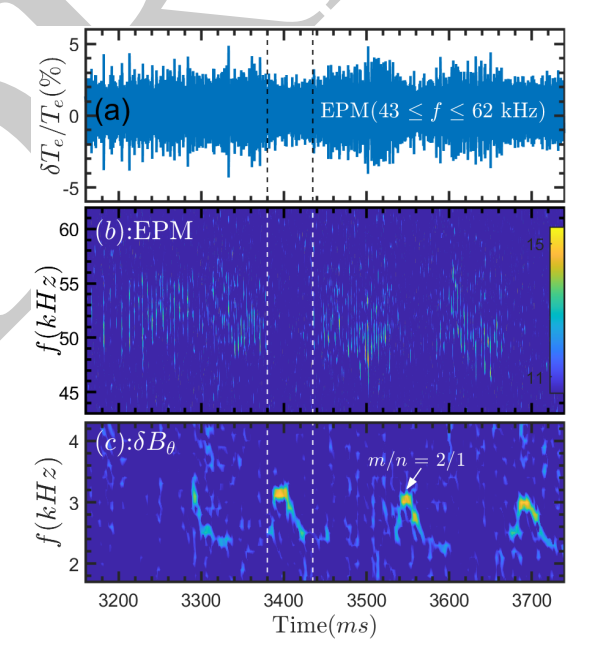


FIG. 9: The EPM instability and the m/n = 2/1 tearing mode are observed to be excited interactively. Panels (a) and (b) present the filtered ECE signal and its corresponding spectrogram, respectively, while panel (c) displays the spectrogram of the edge magnetic signal.

E. Relationship with tearing modes

The relationship between EPM and m/n=2/1 tearing mode is investigated as shown in figure 9. The EPM resides radially between 2.02 and 2.07 m, while the q=2 surface is at $R\approx 2.02$ m at $t\approx 3.4$ s, following the excitation of the tearing mode instability. The EPM instability and the m/n=2/1 tearing mode are observed to be excited interactively. Following the EPM's excitation, the core electron temperature T_{e0} increases by $\Delta T_{e0}/T_{e0}\approx 7\%$, while the change in S_n is significantly smaller, at $\Delta S_n/S_n\simeq 1\%$. The EPM is fully suppressed when the tearing mode amplitude reaches its maximum. As the frequency of the tearing mode is swept downward, a corresponding gradual increase in the fluctuation amplitude of EPM instability is observed.

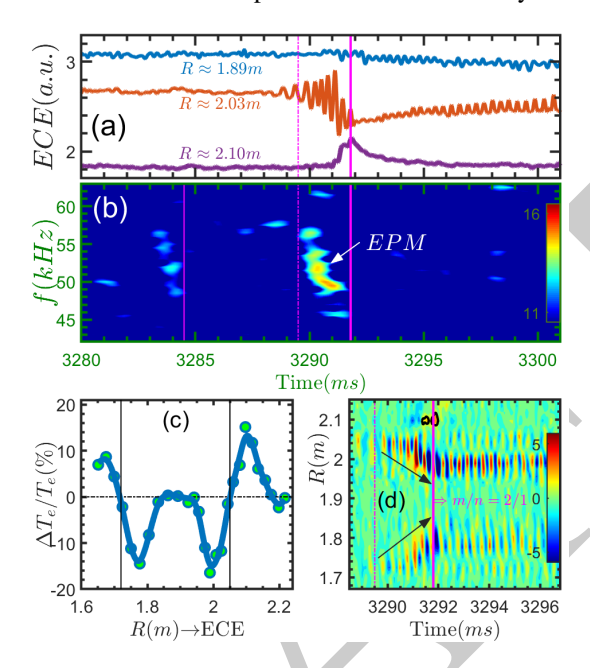


FIG. 10: The relationship among the downward chirps of EPM instability, the burst of off-axis collapse event and the excitation of m/n=2/1 tearing mode. (a) the raw ECE signals at three different radial positions, (b) spectrogram of ECE signal at $R\approx 2.03~m$ for the EPM instability, (c) relative alteration of $\Delta T_e/T_e$ for the off-axis collapse event (magnetic axis $R_0\approx 1.89m$: $\Delta T_e/T_e\approx 0\%$), (d) time evolution of $\delta T_e/T_e$ along the major radius to demonstrate the excitation of tearing modes instability.

The relationship between the downward chirps of EPM and the excitation of m/n=2/1 tearing mode is demonstrated in figure 10. Two examples of EPM chirp events are selected, and a clear off-axis collapse event is observed in the second case, which occurred at $t\approx 3291$ ms. The outward decrease in electron temperature (T_e) in the annular regions of the LFS (1.94 $\le R \le 2.05$ m) and HFS (1.72 $\le R \le 1.84$ m) is associated with the q=2 inversion surface. This rational surface is located at $R\approx 1.72$ m on the HFS and $R\approx 2.05$ m on the LFS respectively (the magnetic axis is located at $R_0 \le 1.9$ m). A precursor mode is clearly observed before the off-axis collapse event [30–33], which occurs nearly simultaneously with the downward chirp of the EPM instability. As indicated by the black arrows in figure 10(d), the radial coverage of precursor mode expands inward. Following the excitation of the tearing mode, the q=2 rational surface moves to $R\approx 1.75$ m on the HFS and $R\approx 2.02$ m on the LFS.

III. CONCLUSION AND DISCUSSION

The upward sweeping RSAEs and downward chirping EPM instabilities are clearly observed near the q=2 surface on the EAST tokamak, and their frequencies separated by the BAE eigenmode frequency. Within a single plasma discharge, the excitation conditions for SAW and EPM instabilities are compared, and it is found that the contributions of fast ions to these modes are substantially different. The radial extent of the SAW is wider than that of the EPM, and the EPM is located farther from the plasma center. The EPM is located at radial position of $2.02 \le R \le 2.1$ m, with normalized minor radius of $0.2 \le \rho \le 0.5$. The growth rates of $\gamma/\omega_0 > 10\%$ is observed for the EPM instability, and the maximum temperature fluctuation of $\delta T_e/T_e \ge 5\%$ is observed. The burst period of the EPM downward chirp is modulated by variations in the electron density, and a decrease in this period leads to the ejection of more fast ions from the plasma. The plasma confinement is unaffected by modifications to the EPM burst period, whereas the $\omega_{E\times B}$ values on either side of the q=2 surface differ significantly. Additionally, the increase in electron temperature T_e during EPM instability excitation suggests the involvement of zonal flow in turbulence suppression. The EPM instability and the m/n=2/1 tearing mode are

IAEA-CN-316/ID: 2894

observed to be excited interactively. A precursor mode is clearly observed during the transition phase, which occurs nearly simultaneously with the downward chirp of the EPM instability. This relationship reveals that the EPM might play a significant role in modifying the current profile.

Acknowledgements

This work was supported by National Magnetic Confinement Fusion Science Program of China under Contract No 2024YFE03170001, National Nature Science Foundation of China under Grant Nos. 12575216 and 12175271.

- [1] L. Chen and F. Zonca, Reviews of Modern Physics 88, 015008 (2016).
- [2] Y. Todo, Reviews of Modern Plasma Physics 3, 1 (2019).
- [3] M. Salewski *et al.*, Nuclear Fusion **65**, 043002 (2025).
- [4] F. Zonca et al., Physics of Plasmas 9, 4939 (2002).
- [5] K. McGuire et al., Physical Review Letters 50, 891 (1983).
- [6] L. Chen, R. B. White, and M. N. Rosenbluth, Physical Review Letters 52, 1122 (1984).
- [7] B. Coppi and F. Porcelli, Physical Review Letters 57, 2272 (1986).
- [8] R. Betti and J. Freidberg, Physical Review Letters 70, 3428 (1993).
- [9] G. T. A. Huysmans et al., Nuclear Fusion 39, 1489 (1999).
- [10] G. Matsunaga et al., Physical Review Letters 103, 045001 (2009).
- [11] W. W. Heidbrink et al., Plasma Physics and Controlled Fusion 53, 085028 (2011).
- [12] M. Okabayashi et al., Physics of Plasmas 18, 056112 (2011).
- [13] H. Li et al., Nuclear Fusion 62, 026013 (2022).
- [14] K. Shinohara et al., Nuclear Fusion 41, 603 (2001).
- [15] E. D. Fredrickson et al., Physics of Plasmas 13, 056109 (2006).
- [16] A. Bierwage et al., Nuclear Fusion 57, 016036 (2017).
- [17] L. M. Yu et al., Europhysics Letters 138, 54002 (2022).
- [18] M. H. Li et al., Nuclear Fusion 62, 126055 (2022).
- [19] H. Du et al., Nuclear Fusion 58, 066011 (2018).
- [20] B. N. Breizman and S. E. Sharapov, Plasma Physics and Controlled Fusion 53, 054001 (2011).
- [21] W. Chen et al., Nuclear Fusion 54, 104002 (2014).
- [22] L. Xu et al., Nuclear Fusion 61, 076005 (2021).
- [23] T. S. Hahm and K. H. Burrell, Physics of Plasmas 2, 1648 (1995).
- [24] K. H. Burrell, Physics of Plasmas 4, 1499 (1997).
- [25] R. C. Wolf, Plasma Physics and Controlled Fusion 45, R1 (2003).
- [26] J. W. Connor et al., Nuclear Fusion 44, R1 (2004).
- [27] A. R. Field et al., Plasma Physics and Controlled Fusion 51, 105002 (2009).
- [28] R. E. Bell et al., Physics of Plasmas 17, (2010).
- [29] G. Brochard et al., Physical Review Letters 132, 075101 (2024).
- [30] M. Xu et al., Nuclear Fusion 59, 084005 (2019).
- [31] M. Xu et al., Nuclear Fusion 60, 112005 (2020).
- [32] M. Xu et al., Nuclear Fusion 61, 106008 (2021).
- [33] M. Xu et al., Acta Physica Sinica 72, 215204 (2023).